



Published in final edited form as:

Mol Imaging Biol. 2010 ; 12(1): 35. doi:10.1007/s11307-009-0234-z.

Feasibility of Whole-Body Functional Mouse Imaging Using Helical Pinhole SPECT

Scott D. Metzler¹, Sreekanth Vemulapalli², Ronald J. Jaszczak³, Gamal Akabani³, and Bennett B. Chin³

¹ Department of Radiology, University of Pennsylvania, 3400 Spruce St., Philadelphia, PA 19104, USA

² School of Medicine, Duke University Medical Center, Durham, NC 27710, USA

³ Department of Radiology, Duke University Medical Center, DUMC-3949, Durham, NC 27710, USA

Abstract

Purpose—Detailed *in vivo* whole-body biodistributions of radiolabeled tracers may characterize the longitudinal progression of disease, and changes with therapeutic interventions. Small-animal imaging in mice is particularly attractive due to the wide array of well characterized genetically and surgically created models of disease. Single Photon Emission Computed Tomography (SPECT) imaging using pinhole collimation provides high resolution and sensitivity, but conventional methods using circular acquisitions result in severe image truncation and incomplete sampling of data which prevent the accurate determination of whole-body radiotracer biodistributions. This study describes the feasibility of helical acquisition paths to mitigate these effects.

Procedures—Helical paths of pinhole apertures were implemented using an external robotic stage aligned with the axis of rotation (AOR) of the scanner. Phantom and mouse scans were performed using helical paths and either circular or bi-circular orbits at the same radius of rotation (ROR). The bi-circular orbits consisted of two 360-degree scans separated by an axial shift to increase the axial field of view (FOV) and to improve the complete-sampling properties.

Results—Reconstructions of phantoms and mice acquired with helical paths show good image quality and are visually free of both truncation and axial-blurring artifacts. Circular orbits yielded reconstructions with both artifacts and a limited effective FOV. The bi-circular scans enlarged the axial FOV, but still suffered from truncation and sampling artifacts.

Conclusions—Helical paths can provide complete sampling data and large effective FOV, yielding 3D full-body *in vivo* biodistributions while still maintaining a small distance from the aperture to the object for good sensitivity and resolution.

Keywords

pinhole; single photon emission computed tomography SPECT; helical; small-animal

Corresponding author: Scott D. Metzler, Tel. 215-662-7773, FAX 215-573-3880, metzler@mail.med.upenn.edu.

Manuscript significance: Helical high-resolution small-animal SPECT provides whole-body biodistribution data without reconstruction artifacts from incomplete sampling. These biodistributions can facilitate the testing of novel radiotracers in pre-clinical studies for drug development. In addition, whole-body radiotracer biodistribution can be performed sequentially, and thus, used to evaluate radiolabelled cell migration in the development of novel cellular therapies.

Introduction

In vivo longitudinal biodistribution studies in mice have several benefits over traditional methods which determine radiotracer biodistribution by sacrificing a subset of subjects at different time points. Non-invasive longitudinal studies allow a particular animal to serve as its own control, which may produce a more rigorous result with fewer mice. Several other *in vivo* processes, such as cell migration after radiolabeling, are also most accurately assessed with sequential imaging. Finally, information from longitudinal studies may also be highly relevant if the effects of a novel therapy are to be assessed in a clinical trial.

Whole-body small-animal Single Photon Emission Computed Tomography (SPECT) uses pinhole collimation for high image magnification and high spatial resolution. Pinhole collimation has high sensitivity and high resolution when the object may be brought near the aperture, or when there is a small radius of rotation (ROR) of the pinhole aperture (1,2), which is affixed to the gamma camera, about the axis of rotation (AOR), which is typically centered on the object. These characteristics have made pinhole SPECT a subject of active research for small-animal imaging (1,3–33), including helical pinhole SPECT (15,20,21,26,27,31–33). For tomographic image reconstruction, the inversion of the set of 2D projection images into a 3D distribution requires that the Kirillov-Tuy (34,35) condition be met. This requires all planes through all points in the object to intersect the path of the pinhole aperture; use of circular orbits with pinhole collimator does not meet the Kirillov-Tuy condition. In addition, a circular orbit may truncate a large portion of the subject mouse if high magnifications are used. Helical paths, however, can allow the Kirillov-Tuy condition to be met while maintaining high magnification and high sensitivity. The same sampling properties exist in x-ray computed tomography (CT). The severity of the sampling problem, however, is much less in x-ray CT than in SPECT; the full opening angle of the cone of photons emitted from the x-ray tube is only about 2 degrees for x-ray CT whereas pinhole SPECT accepts photons within about a 90–120 degree cone as they enter through the pinhole (1,15,36).

Materials and Methods

Description of System

A clinical SPECT system (Triad-XLT, Trionix Research Laboratories, Inc., Twinsburg, OH 44087) capable of circular rotation was used for all projection acquisitions. A single pinhole collimator (focal length of 165 mm) was mounted on one out of three gamma cameras, each of which had a rectangular field of view of 400 mm transaxially and 22 cm axially. When a matching set of pinhole collimators (focal lengths of 200 mm) became available, all three heads used pinhole collimation. The apertures for all studies were made from tungsten with a 1.0 mm diameter and a 100-degree full-acceptance angle.

An external linear stage was aligned with the axis of rotation (AOR) of the scanner (Fig. 1) with an accuracy of about 0.01 degrees (20). It moved the mouse axially while the scanner rotated. The combined effective path of the aperture was helical (15).

Two or three pinhole collimators acquiring simultaneously provide good sampling completeness; a single collimator does not (15). Consequently, when only the single collimator was available, data were acquired in two passes: acquisition with the pinhole aperture completing a 360-degree rotation beginning at (i) $\varphi = 0$ degrees and (ii) $\varphi = 180$ degrees; this is equivalent to two-headed operation.

Phantom Studies

An ultra micro cold-disk phantom (Model ECT/DEF/UMMP, Data Spectrum Corp., Hillsborough, NC 27278) (Fig. 2) was imaged by acquiring data from all three heads with the

pyramid collimators. The disk thicknesses were 1.6 mm, alternating between hot and cold disks. The phantom was filled with about 25 mCi (920 MBq) of aqueous ^{99m}Tc pertechnetate (20% energy window). This amount of activity is higher than often used in small-animal imaging, but allows for high-count acquisitions that are useful for artifact identification in phantom images; the high count rate does not impact sampling completeness, which leads to axial blurring, but does impact image noise. A scan of 180 views/camera (256×128 bins; 1.78 mm edge length) was acquired for a circular orbit in step-and-shoot mode with ROR of 34 mm, where the ROR is measured from the AOR to the aperture plane. Each view was 20 sec. in duration, for a total of 3600 sec. of acquisition. A second scan was acquired using a helical path with pitch of 49 mm (the linear stage moved continuously while the scanner rotated in step-and-shoot mode); all other parameters were the same. The helical pitch was chosen so that the region of interest (i.e., the phantom) began the scan entirely on one side of the central plane of the collimators (i.e., the plane perpendicular to the AOR containing the center points of the apertures) and completed the scan entirely on the opposite side of that plane; all phantom and mouse studies described herein similarly used the axial field of view to determine the helical pitch. The data were reconstructed using an ordered-subset expectation-maximization (OSEM) algorithm (37) that modeled penetrative sensitivity (9) and the penetrative point-spread function (11). The voxels had edge length of 0.5 mm (volume of 125 microliters). A total of 10 iterations with 4 subsets were performed.

A second phantom study was performed using the same scanner and collimation, but with a hot-rod phantom (Model ECT/DLX/UMMP, Data Spectrum Corp., Hillsborough, NC). The phantom had 6 sectors of rods with the following diameters: 0.75, 1.0, 1.35, 1.7, 2.0, and 2.4 mm. The helical path had a pitch of 50 mm. Scanning and reconstruction protocols were similar to the first phantom study.

^{99m}Tc MDP Mouse Bone Scan

A 30-gram mouse was injected with 7 mCi (260 MBq) of ^{99m}Tc -labeled methylene diphosphonate (MDP) intravenously. For imaging, the mouse was induced and maintained under general anesthesia using 2–4% isoflurane. Images were obtained within 4 hours of injection using the single pinhole collimator. A scan of 180 views/camera (256×128 bins; 1.78 mm edge length) was acquired for a circular orbit with ROR of 27 mm. Each view was 10 sec. in duration, for a total acquisition time of 1800 sec. A second scan was acquired using a helical path with pitch of 93 mm, simulating two-headed operation (See “Description of System”). The data were reconstructed using a $80 \times 80 \times 240$ grid of 0.5-mm-edge voxels. A total of 10 iterations with 4 subsets were performed.

Sulfur Colloid Mouse Scan

A 20-gram mouse injected with 12.0 mCi (440 MBq) of ^{99m}Tc -labeled sulfur colloid intravenously. Imaging was performed under general anesthesia using isoflurane as above. Images were acquired using the three pyramidal collimators. The helical scan was acquired with 240 views (3-degree step; 10 s/view) over two revolutions (i.e., 720-degrees; 2400 sec. of total acquisition). The pitch was 41.5 mm/revolution; the total axial translation of the mouse was 83.0 mm. The circular scan was completed with two revolutions and with a 27.7 mm shift between revolutions to increase the axial field of view (FOV). The data were reconstructed using an $80 \times 80 \times 240$ grid of 0.5 mm voxels. A total of 10 iterations with 4 subsets were performed.

Calculation of Average Attenuation

The average attenuation due to self-absorption within a cylinder was calculated for both circular and helical paths for a linear attenuation constant of 0.15 mm^{-1} (i.e., Tc-99m in water) (38). The average attenuation is herein defined as:

$$\text{Avg. Atten.} = 1 - \frac{N_{w\text{-atten}}}{N_{wo\text{-atten}}}, \quad (1)$$

where $N_{w\text{-atten}}$ and $N_{wo\text{-atten}}$ are the number of expected counts with and without attenuation, respectively. Two source configurations were considered. The first was a thin disk source (i.e., cylinder with zero length). The length of the helical path for this source was determined by starting the path as the disk (or central slice of the cylinder) enters the field of view (FOV) and ending just as it completely exits the FOV:

$$L = D(1 + \csc \frac{\alpha}{2}) \tan \frac{\alpha}{2}, \quad (2)$$

where D is the diameter of the cylinder and a is the acceptance angle of the pinhole. The second source was a cylinder with length equal to $2L$. The circular orbit was centered on this source whereas the helical path covered the central region from $-L/2$ to $L/2$.

Results

The reconstructions of the cold-disk phantom are shown in the top row of Fig. 3 (Left: helical path. Right: circular orbit). In the lower row, the activity profiles for the central sagittal slices of the helical path (left) and the circular path (right) are shown. This phantom demonstrates the axial blurring that occurs for circular orbits. Only the central three hot disks can be visualized. The first non-central disks show blurring as can be seen from their reduced magnitudes in the profile. With the helical path, there is no evidence of axial blurring (Fig. 3, left). The profile shows very good separation of these 1.6 mm-thick disks and a very uniform magnitude for them throughout the phantom. Importantly, quantitative accuracy is improved compared to the circular orbit.

In addition, this demonstrates truncation artifacts for circular orbits at the outer edges of the disks furthest from the center (Fig. 3; top right). This artifact is due to the proximity of the pinhole to the phantom, which helps to achieve good resolution and sensitivity, but reduces the FOV. Using the helical path (Fig. 3, top left), there is no evidence of truncation artifacts in the reconstruction, even though individual raw data projections are truncated. This is because there is complete information in the data set for the volume of the cylinder.

Fig. 4 shows transaxial slices of the hot-rod phantom. The left image shows the central slice, which is 0.5 mm thick. The right images show 10 central slices (5.0 mm thick) added to reduce noise. Both images are for 10 iterations. All sectors have distinguishable rods; the smallest sector has 0.7 mm-diameter rods.

The reconstructions of the mouse bone scan are shown in Fig. 5. The reconstructions are shown for two-head helical (left), one-head helical (center), and one-head circular (right). The single-headed acquisition (center) demonstrates the effect of incomplete sampling with blurring in the posterior skull. The circular orbit shows less blurring in this area, but blurring is present in the vertebral bodies of the lower thoracic spine at the inferior edge of the FOV.

The reconstructions of the sulfur colloid scans are shown in Fig. 6. The helical scan is shown on left. To the right of the helical scan is the bi-circular scan. The two scans on the right are the individual circular scans. On the bi-circular scan, blurring and truncation artifacts are seen at the superior and inferior edges of the FOV (superior skull and inferior tail vertebral bone marrow). On the circular scans, these artifacts are again apparent at the edges of the FOV.

Incidentally seen is activity within the blood pool, probably due to relatively large amount of sulfur colloid that is incompletely extracted by the mouse reticuloendothelial system. Faint lung, major abdominal vessel (aorta and inferior vena cava), kidney and bladder activity are also seen in the lateral projections of the supplemental image in cine format.

The average attenuation results are plotted in Fig. 7. The top row shows results from a thin-disk source. This source is centered on the plane of the pinhole aperture. For the helical path, the plane enters and leaves the field of view. The bottom row shows results for a long cylinder. The cylinder's length is twice that of the helical-path's axial translation; this length makes it sufficiently long that the source is always axially truncated in both directions.

Discussion

Using a small ROR with pinhole SPECT improves resolution and sensitivity. However, using only a circular orbit yields axial blurring and a reduced FOV. These problems are mitigated with helical paths.

Pinhole SPECT allows both high sensitivity and high resolution for small objects when the ROR is small. These improvements are due to high magnification, which reduces the axial FOV. The use of helical pinhole SPECT provides complete sampling over an extended axial range, while allowing for high resolution and high sensitivity. Further, helical orbits can be adjusted to give longer view times near the region of interest and shorter view times outside that region to improve counts where desired, but to reduce blurring artifacts. On the other hand, a circular orbit can provide higher average sensitivity if the axial FOV is small because the entire FOV remains visible to the scanner throughout the acquisition and the axial-blurring artifacts are small within that narrow FOV. Some scanner's, such as U-SPECT-1 (41), focus numerous pinholes from different axial planes over a small FOV. This can give large sensitivity over this small FOV and it can give good axial sampling.

The use of helical paths does not preclude good transverse resolution as demonstrated by Fig. 4. Even a single transverse slice shows good resolution: all sectors including the 0.7 mm-diameter rods are resolved.

The choice of helical pitch is important for obtaining complete sampling over the entire field of view. Generally, our approach is to determine the axial travel needed by the stage so that the entire object crosses the central plane of the collimation during the scan. The motivation for this approach is the sampling rule of Tuy (35): all planes through the object must intersect the path of the pinhole apertures. It is possible that this pitch can be too large to yield complete sampling since the scan would out-run the Tam window (39). It is straight forward to determine the maximum pitch when a single camera is used, based on the Tam window; that pitch is twice the ROR times the ratio of the axial length of the detector to the collimator's focal length. It is less clear when multiple detectors are used, but multiple detectors always improve sampling. Numerical methods can be used to evaluate the maximum pitch that gives complete sampling in the case of multiple collimators (40). The choice of the number of steps yields a tradeoff between axial resolution and live time (i.e., the amount of time acquiring data rather than rotating the system) (31). We have generally found 120–180 steps to be a good overall choice for balancing live-time with the requirements for good axial and transaxial resolution.

Implementation of helical pinhole SPECT is relatively inexpensive (~\$30,000 (21)) if a general-purpose SPECT scanner can be used. Pinhole collimators can be mounted on this scanner. A robotic linear stage can be purchased and aligned using published methods. Reconstruction is possible with suitable iterative algorithms that have been generalized for helical paths.

With the use of a mouse holder, the robotic stage provides a convenient mechanism for positioning the subject for both circular and helical scans. The holder is easily aligned with the axis of rotation. When setting up a scan, there is no need to adjust the transaxial dimensions. The axial dimension needs to be adjusted depending on the scan type and the size of the animal. However this is relatively straight forward since it is the only dimension that needs to change from mouse to mouse.

The pursuit of high resolution and high sensitivity in pinhole imaging inherently conflicts with complete-sampling properties. As the ROR is decreased to improve both sensitivity and resolution, the sampling completeness worsens (15). Helical paths of pinhole apertures allow the improvements in sensitivity and resolution that are achieved with small RORs to be complemented with complete sampling over an extended axial FOV. The cost of helical paths compared with circular orbits is that complete sampling is gained at the expense of central-plane sensitivity.

Fig. 7 shows that helical-path and circular-orbit pinhole SPECT have different attenuation properties. The top row of the figure shows that if one considers only a narrow axial slice, there is reduced attenuation for circular orbits, compared with helical paths. The reason for this is that the photons for the circular orbit remain in the plane of the source, compared with those photons for the helical path, which also have an axial component. That axial component increases the path length in attenuating material, increasing attenuation. In contrast, when one considers a long cylinder as the source, there is reduced average attenuation for the helical path since the pinhole has higher sensitivity when it is near a point, which is also when it has low attenuation.

Conclusion

When the ROR is reduced in pinhole SPECT, higher sensitivity and resolution are achieved. However, there is severe axial blurring and truncation in reconstructions of circular orbits. Helical paths decrease axial blurring and increase the effective FOV while maintaining a small ROR; this can produce more quantitatively accurate whole-body biodistributions in small-animal imaging while maintaining high resolution and sensitivity. Helical pinhole SPECT is a feasible method to obtain high sensitivity and resolution whole-body imaging overcoming the limitations of truncation and limited field of view from circular orbits.

Acknowledgments

This research was supported by the National Institute for Biomedical Imaging and Bioengineering of the National Institutes of Health (NIH) under Grants R01-EB-001910 and R33-EB-001543. Experimental data were acquired using shared instrumentation funded by the National Center for Research Resources of the NIH under Grant S10 RR15697. S. Vemulapalli was supported in part by a Howard Hughes Medical Student Research Training Fellowship grant. The authors thank Dr. Timothy Turkington for the use of the software package 'SPECTER V4.0' for image display and Mr. Kim Greer for experimental and computer assistance. One of the authors (RJJ) is a consultant and officer of Data Spectrum Corporation (DSC) and has an equity interest in DSC.

References and Notes

1. Jaszczak RJ, Li J, Wang H, Zalutsky MR, Coleman RE. Pinhole Collimation for Ultra-High-Resolution, Small-Field-of-View SPECT. *Phys Med Biol* 1994;39:425–437. [PubMed: 15551591]
2. Anger, HO. Radioisotope Cameras. In: Hine, GJ., editor. *Instrumentation in Nuclear Medicine*. Vol. 1. New York: Academic Press; 1967. p. 485-552.
3. Mortimer RK, Anger HO, Tobias CA. The Gamma Ray Pinhole Camera with Image Amplifier. *Convention Record of the Institute of Radio Engineers, Part 9 - Medical and Nuclear Electronics* 1954:2–5.
4. Paix D. Pinhole Imaging of Gamma Rays. *Phys Med Biol* 1967;12(4):489–500. [PubMed: 6061848]

5. Moyer R. A low-energy multihole converging collimator compared with a pinhole collimator. *J Nucl Med* 1974;15(2):59–64. [PubMed: 4810590]
6. Hasegawa B, Kirch D, Stern D, et al. Single-photon emission tomography with a 12-pinhole collimator. *J Nucl Med* 1982;23(7):606–612. [PubMed: 6979615]
7. Palmer J, Wollmer P. Pinhole emission computed tomography: method and experimental evaluation. *Phys Med Biol* 1990;35(3):339–350. [PubMed: 2320666]
8. Weber DA, Ivanovic M, Franceschi D, et al. Pinhole SPECT: An Approach to In Vivo High Resolution SPECT Imaging in Small Laboratory Animals. *J Nucl Med* 1994;35(2):342–348. [PubMed: 8295008]
9. Metzler SD, Bowsher JE, Smith MF, Jaszczak RJ. Analytic Determination of Pinhole Sensitivity with Penetration. *IEEE Trans Med Imag* 2001;20(8):730–741.
10. Tenney C, Tornai M, Smith M, Turkington T, Jaszczak R. Uranium pinhole collimators for 511-keV photon SPECT imaging of small volumes. *IEEE Trans Nucl Sci* 2001;48(4):1483–1489.
11. Metzler SD, Bowsher JE, Greer KL, Jaszczak RJ. Analytic Determination of the Pinhole Collimator's Point-Spread Function and RMS Resolution with Penetration. *IEEE Trans Med Imag* 2002;21(8):878–887.
12. Beekman FJ, McElroy DP, Berger F, Gambhir SS, Hoffman EJ, Cherry SR. Towards *In Vivo* nuclear microscopy: I-125 imaging in mice using micro-pinholes. *E J Nucl Med* 2002;29(7):933–938.
13. Wu MC, Hasegawa BH, Dae MW. Performance evaluation of a pinhole SPECT system for myocardial perfusion imaging of mice. *Med Phys* 2002;29(12):2830–2839. [PubMed: 12512717]
14. Beque D, Nuyts N, Bormans G, Suetens P, Dupont P. Characterization of Pinhole SPECT Acquisition Geometry. *IEEE Trans Med Imag* 2003;22(5):599–612.
15. Metzler SD, Greer KL, Jaszczak RJ. Helical Pinhole SPECT for Small-Animal Imaging: A Method for Addressing Sampling Completeness. *IEEE Trans Nucl Sci* 2003;50(5):1575–1583.
16. Schramm NU, Ebel G, Engeland U, Schurrat T, Behe M, Behr TM. High-resolution SPECT using multipinhole collimation. *IEEE Trans Nucl Sci* 2003;50(3):315–320.
17. Williams MB, Stolin AV, Kundu BK. Investigation of efficiency and spatial resolution using pinholes with small pinhole angle. *IEEE Trans Nucl Sci* 2003;50(5):1562–1568.
18. Accorsi R, Metzler SD. Analytic Determination of the Resolution-Equivalent Effective Diameter of a Pinhole Collimator. *IEEE Trans Med Imag* 2004;23(6):750–763.
19. Meng LJ, Clinthorne NH. A modified uniform Cramer-Rao bound for multiple pinhole aperture design. *IEEE Trans Med Imag* 2004;23(7):896–902.
20. Metzler SD, Greer KL, Bobkov K, Jaszczak RJ. Laser Alignment System for Helical Pinhole SPECT. *IEEE Trans Nucl Sci* 2004;51(3):603–610.
21. Metzler SD, Jaszczak RJ, Patil NH, Vemulapalli S, Akabani G, Chin BB. Molecular Imaging of Small Animals With a Triple-Head SPECT System Using Pinhole Collimation. *IEEE Trans Med Imag* 2005;24(7):853–862.
22. DiFilippo FP, Riffe MJ, Harsch KM, McCabe NP, Heston WD. Detached multipinhole small animal SPECT device with real-time calibration. *IEEE Trans Nucl Sci* 2006;53(5):2605–2612.
23. Funk T, Kirch DL, Koss JE, Botvinick E, Hasegawa BH. A novel approach to multipinhole SPECT for myocardial perfusion imaging. *J Nucl Med* 2006;47(4):595–602. [PubMed: 16595492]
24. Metzler SD, Jaszczak RJ. Simultaneous multi-head calibration for pinhole SPECT. *IEEE Trans Nucl Sci* 2006;53(1):113–120.
25. van der Have F, Beekman FJ. Penetration, scatter and sensitivity in channel micro-pinholes for SPECT: A Monte Carlo investigation. *IEEE Trans Nucl Sci* 2006;53(5):2635–2645.
26. Wang YC, Tsui BMW. Pinhole SPECT with different data acquisition geometries: Usefulness of unified projection operators in homogeneous coordinates. *IEEE Trans Med Imag* 2007;26(3):298–308.
27. Vemulapalli S, et al. Cell therapy in murine atherosclerosis: In vivo imaging with high-resolution helical SPECT. *Radiology* 2007;242(1):198–207. [PubMed: 17185668]
28. Defrise M, Vanhove C, Nuyts J. Perturbative refinement of the geometric calibration in pinhole SPECT. *IEEE Trans Med Imag* 2008;27(2):204–214.
29. DiFilippo FP. Geometric characterization of multi-axis multi-pinhole SPECT. *Med Phys* 2008;35(1):181–194. [PubMed: 18293574]

30. Vunckx K, Beque D, Defrise M, Nuyts J. Single and multipinhole collimator design evaluation method for small animal SPECT. *IEEE Trans Med Imag* 2008;27(1):36–46.
31. Ayan AS. Metzler Axial Resolution of Helical-Orbit Pinhole SPECT With Synchronized and Unsynchronized Motion. *IEEE Trans Nucl Sci* 2008;55(2):524–530.
32. Qian JG, et al. A small-animal imaging system capable of multipinhole circular/helical SPECT and parallel-hole SPECT. *NIM-A* 2008;594(1):102–110.
33. DiFilippo FP. Design and performance of a multi-pinhole collimation device for small animal imaging with clinical SPECT and SPECT-CT scanners. *Phys Med Biol* 2008;53(15):4185–4201. [PubMed: 18635899]
34. Kirillov AA. On a problem of I.M. Gel'fand. *Sov Math Dokl* 1961;2:268–269.
35. Tuy HK. An Inversion Formula for Cone-Beam Reconstruction. *SIAM J Appl Math* 1983;43:546–552.
36. Hsieh J. Investigation of an image artefact induced by projection noise inhomogeneity in multi-slice helical computed tomography. *Phys Med Biol* 2003;48(3):341–356. [PubMed: 12608611]
37. Hudson HM, Larkin RS. Accelerated Image Reconstruction Using Ordered Subsets of Projection Data. *IEEE Trans Med Imag* 1994;13(4):601–609.
38. Hubbell, JH.; Seltzer, SM. Tables of x-ray mass attenuation coefficients and mass energy-absorption coefficients (version 1.02), [online]. National Institute of Standards and Technology; Gaithersburg, MD: 1997. Available: <http://physics.nist.gov/xaamdi>
39. Tam KC, Samarasekera S, Sauer F. Exact cone beam CT with a spiral scan. *Phys Med Biol* 1998;43(4):1015–1024. //red. [PubMed: 9572524]
40. Metzler SD, Bowsher JE, Jaszczak RJ. Geometrical Similarities of the Orlov and Tuy Sampling Criteria and a Numerical Algorithm for Assessing Sampling Completeness. *IEEE Trans Nucl Sci* 2003;50(5):1550–1555.
41. Vastenhouw B, Beekman F. Submillimeter total-body murine imaging with U-SPECT-1. *J Nucl Med* 2007;48(3):487–493. green. [PubMed: 17332628]

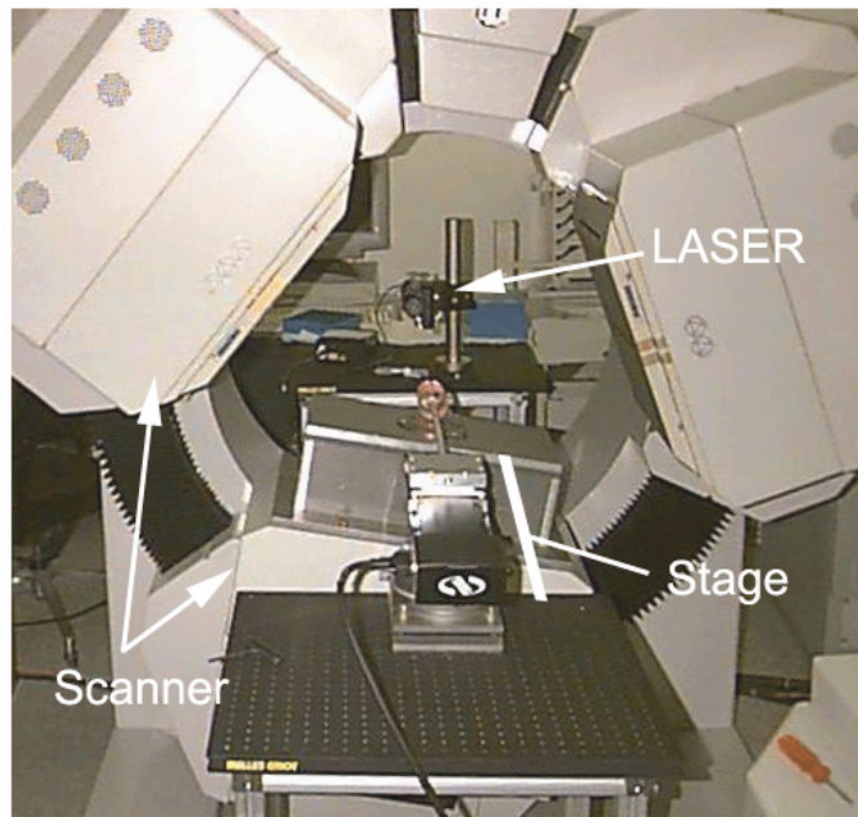


Figure 1. Photograph of scanner with aligned linear stage, but with only one box-type pinhole collimator. The laser, which is behind the scanner, is used to align the stage with the axis of rotation.



Figure 2. Ultra Micro Cold-Disk Phantom. The disks and spacing are 1.6 mm thick and 22 mm in diameter.

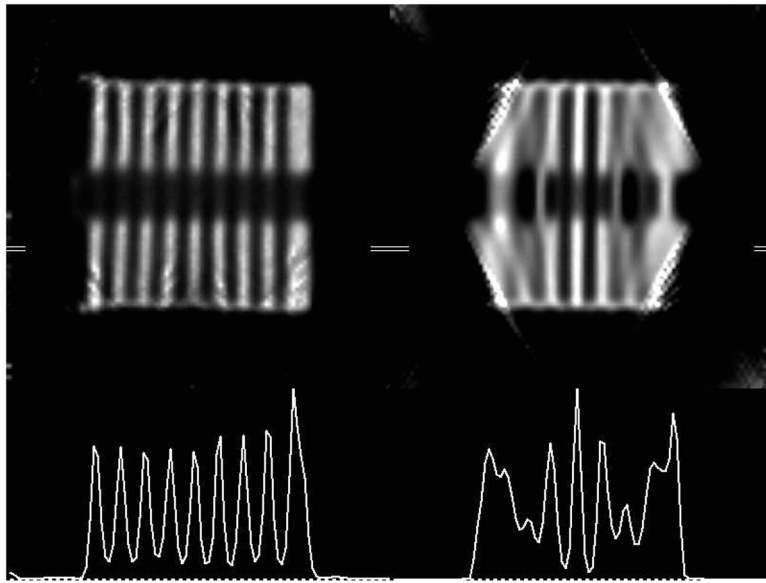


Figure 3. Central sagittal slice of reconstructions (top) with their profiles (bottom) for helical (left) and circular (right) scans. The horizontal line segment indicates the region of the profile. Circular orbit (right) shows truncation artifacts (upper right) and quantitative inaccuracies (lower right) due to incomplete sampling.

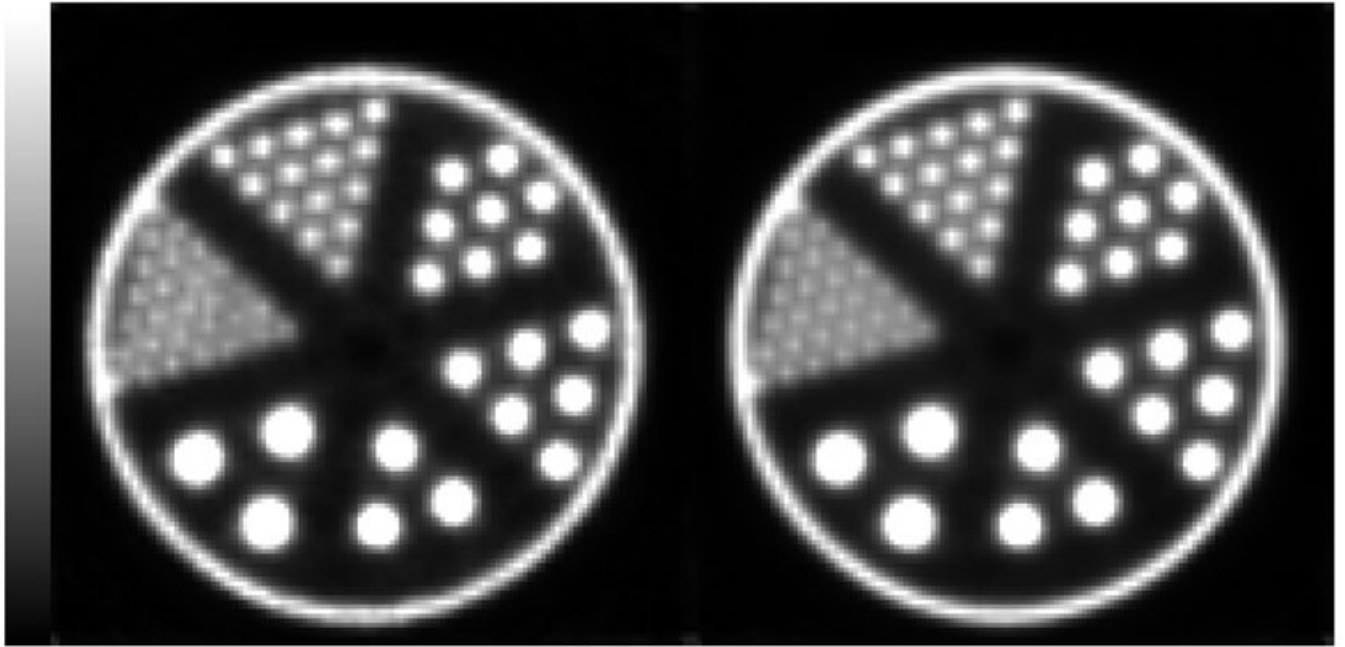


Figure 4. Reconstructed transaxial slices of the Data Spectrum Corp. ECT/HOT/UMMP phantom. The phantom has six sectors of hot rods with diameters: 0.75, 1.0, 1.35, 1.7, 2.0, and 2.4 mm. The left image is for 1 slice (0.5 mm thick); the right image sums 10 slices (5.0 mm thick). Both images are for 10 iterations.



Figure 5. Reprojections of ^{99m}Tc MDP SPECT mouse bone scan using two-camera helical (left), one-camera helical (center), and one-camera circular (right) aperture paths. Clear delineation of small individual structures such as ribs is possible by using helical paths.

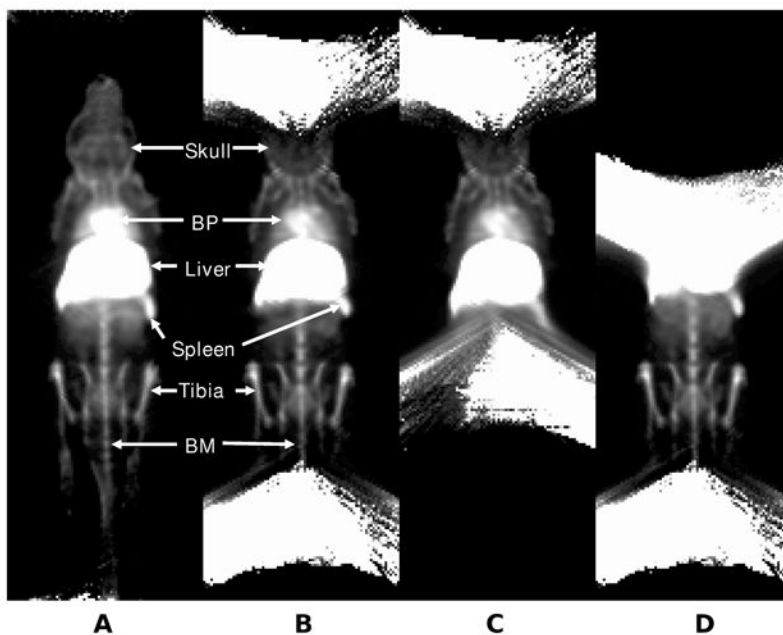


Figure 6.

Reprojections of ^{99m}Tc sulfur colloid SPECT mouse scan. (A) Helical path, (B) circular orbit combining 2 fields of view, (C) circular orbit of the upper FOV, and (D) circular orbit of the lower FOV. Helical acquisition demonstrates preservation of spatial resolution and lack of artifacts at the periphery of the circular orbit fields of view. The bone marrow activity in the skull and tail are clearly seen on the helical-path acquisition, but are not visualized on the circular orbits. The three-dimensional structural relationships and definition of bone marrow within small structures (skull, femur and tibia) are best seen on the lateral re-projections. (Please see supplemental cine showing all re-projections in movie format). BP=cardiac blood pool; BM= bone marrow within the tail vertebra.

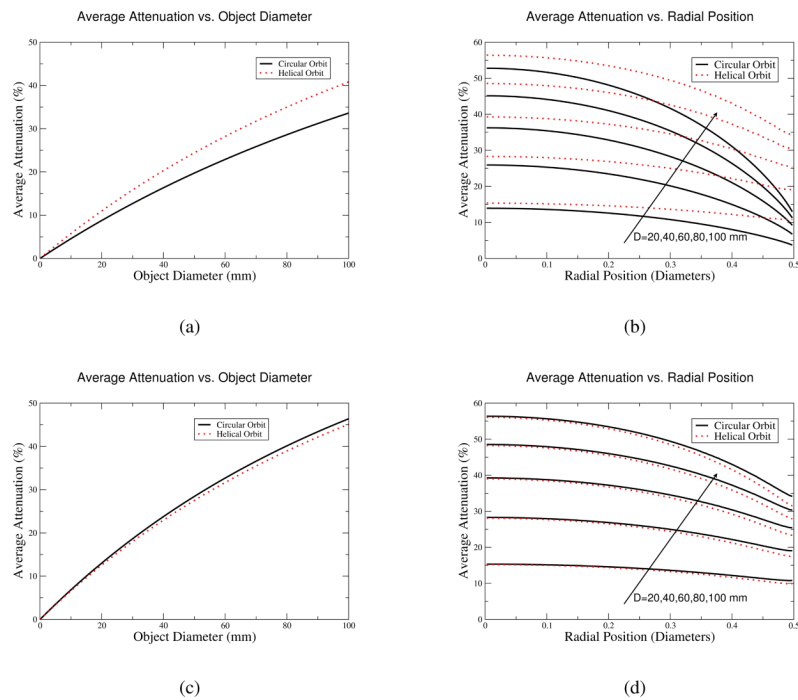


Figure 7.

Average attenuation over a this disk (top) and a cylinder (bottom) for helical paths and circular orbits. Results are shown for the average over the entire region (left) and also as a function of radial position (right) for diameters of 20, 40, 60, 80, and 100 mm; the arrow indicates that the diameter is increasing for the curves as the attenuation increases. Average attenuation for a mouse (approximately 20–25 mm in diameter), is typically less than 15%. Note that helical and circular orbits have comparable attenuation for small animals.